

# Polarization of Sunyaev-Zeldovich signal due to electron pressure anisotropy in galaxy clusters

I. Khabibullin<sup>1,2\*</sup>, S. Komarov<sup>2</sup>, E. Churazov<sup>1,2</sup>, A. Schekochihin<sup>3,4</sup>

<sup>1</sup>Max Planck Institute for Astrophysics, Karl-Schwarzschild-Strasse 1, 85741 Garching, Germany

<sup>2</sup>Space Research Institute (IKI), Profsoyuznaya 84/32, Moscow 117997, Russia

<sup>3</sup>The Rudolf Peierls Centre for Theoretical Physics, University of Oxford, 1 Keble Road, Oxford OX1 3NP, United Kingdom

<sup>4</sup>Merton College, Oxford OX1 4JD, United Kingdom

11 March 2022

## ABSTRACT

We describe polarization of the Sunyaev-Zel’dovich (SZ) effect associated with electron pressure anisotropy likely present in the intracluster medium (ICM). The ICM is an astrophysical example of a weakly collisional plasma where the Larmor frequencies of charged particles greatly exceed their collision frequencies. This permits formation of pressure anisotropies, driven by evolving magnetic fields via adiabatic invariance, or by heat fluxes. SZ polarization arises in the process of Compton scattering of the cosmic microwave background (CMB) photons off the thermal ICM electrons due to the difference in the characteristic thermal velocities of the electrons along two mutually orthogonal directions in the sky plane. The signal scales linearly with the optical depth of the region containing large-scale correlated anisotropy, and with the degree of anisotropy itself. It has the same spectral dependence as the polarization induced by cluster motion with respect to the CMB frame (kinematic SZ effect polarization), but can be distinguished by its spatial pattern. For the illustrative case of a galaxy cluster with a cold front, where electron transport is mediated by Coulomb collisions, we estimate the CMB polarization degree at the level of  $10^{-8}$  ( $\sim 10$  nK). An increase of the effective electron collisionality due to plasma instabilities will reduce the effect. Such polarization, therefore, may be an independent probe of the electron collisionality in the ICM, which is one of the key properties of a high- $\beta$  weakly collisional plasma from the point of view of both astrophysics and plasma theory.

**Key words:** ICM, plasma, magnetic field, SZ, polarization

## 1 INTRODUCTION

The cosmic microwave background (CMB) radiation in the direction of galaxy clusters is distorted due to Compton scattering of the CMB photons off the hot electrons of the intracluster medium (ICM), as first predicted by Sunyaev & Zeldovich (1972). These distortions have a characteristic spectral shape determined by the relative contributions of the thermal (tSZ, Sunyaev & Zeldovich 1972) and kinematic, i.e., related to the bulk motion of a cluster (kSZ, Sunyaev & Zeldovich 1980), effects. Both are now readily detected by space and ground-based millimetre and sub-mm observatories (e.g., Hasselfield et al. 2013; Bleem et al. 2015; Planck Collaboration et al. 2014).

Importantly, the amplitude of the effect is proportional to the volume-integrated gas pressure of the ICM (which can

be used as a proxy for the cluster’s mass), and its surface brightness does not depend on the distance to the cluster, making the SZ signal an extremely valuable tool for both cosmological and ICM studies (Sunyaev & Zeldovich 1981; Rephaeli 1995; Birkinshaw 1999; Carlstrom, Holder, & Reese 2002; Planck Collaboration et al. 2014). Recently, a high-resolution ( $\sim 5''$ ) mapping of the SZ effect became available owing to the *ALMA* observatory (Kitayama et al. 2016). It allows to study physical scales of  $\sim 20$  kpc at the distance of  $z \sim 0.25$  with the sensitivity  $17 \mu\text{Jy beam}^{-1}$  (at 92 GHz), or  $\sim 100 \mu\text{K}$  at  $5''$  full width at half maximum (Kitayama et al. 2016, see also Young et al. 2015 for MUSTANG/GBT and Adam et al. 2016 for IRAM/NIKA detections).

Because Compton-scattered photons are linearly polarized, the SZ effect also has the potential to reveal itself in the polarization of the CMB radiation (Sunyaev & Zeldovich 1980; Zeldovich & Sunyaev 1980; Sunyaev & Zeldovich 1981). For the net polarization signal from a cluster

\* E-mail: ildar@mpa-garching.mpg.de

not to cancel out after integration over the incident photon momenta, the presence of a quadrupole component in the CMB angular anisotropy (as seen by the electrons in the cluster) is needed (Zeldovich & Sunyaev 1980). Quadrupole anisotropy can be inherent to the CMB radiation itself (Zeldovich & Sunyaev 1980), or can be induced by the motion of the cluster with respect to the CMB, finite-optical-depth effects, or a combination of these (Zeldovich & Sunyaev 1980; Sazonov & Sunyaev 1999; Lavaux et al. 2004; Shimon et al. 2006). Additionally, the local intensity distribution can be distorted by gravitational effects, e.g., the moving-gravitational-lens effect (Gibilisco 1997).

In this paper, we predict yet another potential mechanism of generation of the SZ polarization by electron pressure anisotropies. Such anisotropies are typically produced in a plasma where the Coulomb collision frequencies of the charged particles are small compared to their Larmor frequencies (such a plasma is often called weakly collisional). This is, indeed, the case in the ICM: even for a seemingly small magnetic field ( $\sim 1\mu\text{G}$ ) observed in galaxy clusters (Feretti et al. 2012), Larmor scales are separated from Coulomb mean free paths by many orders of magnitude. Pressure anisotropies can then be driven by evolving magnetic fields via adiabatic invariance, and by heat fluxes (see e.g. Schekochihin & Cowley 2006 and references therein). The amplitude of these anisotropies is likely to be small: first, because plasma motions in the ICM are typically significantly subsonic; second, because even a low anisotropy quickly leads to the development of kinetic microinstabilities. These instabilities (firehose, mirror and, possibly, whistler modes) regulate the anisotropy level by particle scattering off magnetic perturbations. As a result, the anisotropy is kept at the low level of marginal stability (e.g., Kunz, Schekochihin, & Stone 2014; Riquelme, Quataert, & Verscharen 2016; Santos-Lima et al. 2016; see also Kasper, Lazarus, & Gary 2002; Hellinger et al. 2006; Štverák et al. 2008; Bale et al. 2009; Chen et al. 2016 for direct observations in the solar wind, where anisotropies reach  $\gtrsim 1$  level in low ( $\lesssim 1$ ) plasma beta regions). Whether this picture is fully applicable to the intracluster plasma is rather uncertain, and observational techniques offering a peek into plasma microphysics by constraining the effective electron collisionality of the ICM are of interest.

One of the most promising targets for such studies can be galaxy clusters containing shocks and cold fronts, i.e., sharp temperature and density discontinuities associated either with a cold subcluster moving in a host cluster or sloshing of relatively cool gas displaced from a cluster core (Markevitch et al. 2000; see Markevitch & Vikhlinin 2007; Zuhone & Roediger 2016 for reviews). Field-line draping along a cold front interface is believed to be responsible for keeping these substructures from smearing out by thermal conduction and hydrodynamical instabilities (Etori & Fabian 2000; Vikhlinin, Markevitch, & Murray 2001; Vikhlinin & Markevitch 2002, also see Churazov & Inogamov 2004 for an alternative). Along with heat fluxes, these evolving magnetic fields should also produce both ion and electron pressure anisotropies spatially ordered on a macroscopic scale of a cold front. Large-scale anisotropy can also be produced by compression of magnetic field at shocks that form ahead of supersonic cold fronts. Therefore, the polarization signal induced by electron anisotropy can survive

after integration along the line of sight, as opposed to the polarization produced by random turbulent motions.

In the previous work (Komarov et al. (2016b), Paper I hereafter), we demonstrated this for the polarization of cluster thermal bremsstrahlung X-ray emission. We used a trans-sonic cold front with a bow shock as a numerical model to study the total polarization resulting from compression, field-line stretching and heat fluxes. Here, we take advantage of the same numerical setup to predict the corresponding CMB polarization and to compare it with the expected CMB polarization in the direction of galaxy clusters induced by other effects. For our illustrative case, the amplitude of anisotropy-induced polarization turns out to be at the same level ( $\sim 10$  nK) as polarization induced by the motion of the subcluster and by finite-optical-depth effects. However, different spatial or spectral shapes of the signals could facilitate the differentiation between them.

The paper is structured as follows. In Section 2, we describe the generation of electron pressure anisotropies in the ICM. In Section 3, we calculate the corresponding CMB polarization and compare it with polarization signals due to other effects. We present the predicted polarization signal for a simulated cold front in Section 4, and discuss the feasibility of its detection in Section 5. The conclusions are given in Section 6.

## 2 PRESSURE ANISOTROPIES IN THE ICM

The ICM is a hot ( $T \sim 10$  keV), tenuous ( $n \sim 10^{-3}$  cm $^{-3}$ ) weakly magnetized plasma. The typical magnetic-field strength,  $B \sim$  a few  $\mu\text{G}$  (see Carilli & Taylor 2002; Feretti et al. 2012)), corresponds to the ratio of thermal to magnetic-energy densities (plasma beta)  $\beta_{pl} = 8\pi nT/B^2 \sim 100$ . This immediately implies that for all particle species  $s$ , the mean free paths  $\lambda_s$  set by Coulomb collisions greatly exceed the corresponding Larmor radii  $\rho_s$  by orders of magnitude. For a fiducial set of the ICM parameters, one gets (Spitzer 1962; Sarazin 1988):

$$\lambda_s = \lambda_{mfp} \approx 20 \text{ kpc} \left( \frac{T}{8 \text{ keV}} \right)^2 \left( \frac{n}{10^{-3} \text{ cm}^{-3}} \right)^{-1} \quad (1)$$

for both protons and electrons, and

$$\rho_p \sim 4 \times 10^{-12} \text{ kpc} \left( \frac{T}{8 \text{ keV}} \right)^{1/2} \left( \frac{B}{1 \mu\text{G}} \right)^{-1}, \quad (2)$$

$$\rho_e \sim 10^{-13} \text{ kpc} \left( \frac{T}{8 \text{ keV}} \right)^{1/2} \left( \frac{B}{1 \mu\text{G}} \right)^{-1} \quad (3)$$

for the proton and electron Larmor radii, respectively.

Therefore, Coulomb collisions are ineffective in keeping particle distributions isotropic, and they become gyrotropic, i.e., axially symmetric around the field lines. In this case, a difference between the parallel and perpendicular (to the magnetic-field line) pressure can develop. It is characterized by the degree of anisotropy

$$\Delta_s \equiv \frac{p_{\perp s} - p_{\parallel s}}{p_s}, \quad (4)$$

where  $p_{\perp s}$  and  $p_{\parallel s}$  are the perpendicular and parallel pressure, respectively, while  $p_s = \frac{1}{3}p_{\parallel s} + \frac{2}{3}p_{\perp s}$  is the mean pressure, all for particle species  $s$ . Apart from adiabatic invari-

ance, heat fluxes can provide an additional source of pressure anisotropy.

The value of  $\Delta_s$  is set by the balance between the rate of isotropisation by particle scattering (either by Coulomb collisions or scattering off magnetic perturbations produced by plasma instabilities) and the rate at which anisotropy is driven by changing magnetic fields, changing particle density, and heat fluxes, as described by the so-called modified (by the inclusion of isotropic collisions and heat fluxes) CGL equations (Chew, Goldberger, & Low 1956; Schekochihin et al. 2010). From them, it follows that

$$\Delta_s = \frac{p_{\perp s} - p_{\parallel s}}{p_s} \approx \frac{1}{\nu_s} \left[ \frac{1}{B} \frac{dB}{dt} - \frac{2}{3} \frac{1}{n_s} \frac{dn_s}{dt} + \frac{4\nabla \cdot (q_s \mathbf{b}) - 6q_s \nabla \cdot \mathbf{b}}{15p_s} \right], \quad (5)$$

where  $\nu_s$  is the effective collision frequency,  $B$  the magnetic-field strength,  $\mathbf{b}$  the magnetic-field unit vector,  $n_s$  is the number density of the particle specie  $s$ . The total parallel heat flux is  $q_s = q_{\perp s} + q_{\parallel s}/2 = (5/6)q_{\parallel s}$ , where  $q_{\perp s}$  and  $q_{\parallel s}$  are the parallel flux of the ‘‘perpendicular internal energy’’ and the parallel flux of the ‘‘parallel internal energy’’ respectively (Schekochihin et al. (2010); Paper I). The first two terms on the right side of equation (5) correspond to the conservation of the magnetic moment of a charged particle (the first adiabatic invariant) in a weakly collisional plasma with evolving magnetic fields, while the last term is the contribution of the parallel heat flux.

The collision timescales in the ICM are still short enough compared to the timescales set by thermal conduction and fluid motions feeding the anisotropy for  $\Delta_s$  to be low, and  $p_{\parallel s} - p_{\perp s} \ll p_{\perp s} \approx p_{\parallel s} \approx p_s$ . Note that the electron Coulomb collision frequency declines steeply as the velocity of a particle increases,  $\nu_e(v) \propto v^{-3}$  (e.g., Spitzer 1962). This means that one might expect a somewhat higher level of anisotropy for suprathermal electrons. However, the number of such electrons drops even more rapidly ( $\propto v^2 e^{-m_e v^2/2T}$ ), so their influence on the amplitude of the effects under consideration stays small, causing an amplification by a factor of the order of unity at most.

The contribution of different driving terms  $\Delta_{B,n;s}$  (changing  $B$  and  $n$ ) and  $\Delta_{T;s}$  (heat fluxes) to the total anisotropy can be estimated as (e.g. Paper I)

$$\Delta_{B,n;s} \sim \frac{u}{v_{\text{th},s}} \frac{\lambda_s}{L_u}, \quad (6)$$

$$\Delta_{T;s} \sim \frac{\lambda_s^2}{L_T L_u} \frac{\delta T_s}{T_s}, \quad (7)$$

where parallel (with respect to the magnetic field) fluid motions are characterized by velocity  $u$  at parallel scale  $L_u$ , variations of  $B$  at the parallel scale of the velocity field  $L_B = L_u$ , and parallel temperature gradient  $\nabla_{\parallel} T_s \sim \delta T_s/L_T$  at scale  $L_T$ . The heat flux is given by  $q_s = -\kappa_s \nabla_{\parallel} T_s$ , where thermal conductivity  $\kappa_s \sim n_s v_{\text{th},s} \lambda_s$ ,  $\lambda_s$  is the mean free path and  $v_{\text{th},s}$  the thermal speed.

Under conditions typical for the ICM, the term associated with the magnetic-field changes is likely to dominate the ion anisotropy, while for electrons, the contribution of thermal conduction can be of the same order, depending on the properties of the flow and the relative orientation of

magnetic-field lines and temperature gradients (see, e.g., Komarov et al. 2014). It is the electron pressure anisotropy that primarily determines the expected polarization of both the thermal bremsstrahlung and SZ signals, so in general both anisotropy-driving terms have to be taken into account.

Substituting the parameters typical of a cold front, which is the main example analyzed in this paper, we have  $u \sim v_{\text{th},i}$  (i.e., a nearly sonic flow) and  $L_u \sim R$ , where  $R$  is the cold front’s radius of curvature. Therefore, the expected level of the anisotropy is  $\Delta_{B,n;p} \sim \lambda/R$  for ions and  $\Delta_{B,n;e} \sim 1/40 \times \lambda/R$  for electrons. For a cold front of radius  $R \sim 200$  kpc, using the Coulomb mean free path (1), this results in  $\Delta_{B,n;p} \sim 0.1$  for ions and  $\Delta_{B,n;p} \sim 2.5 \times 10^{-3}$  for electrons. As noted above, the total electron anisotropy may also include a comparable heat-flux contribution: by analyzing our numerical simulation data, we calculate both driving terms in Section 4.

It should be noted that the maximum total anisotropy  $\Delta_e + \Delta_p$  is bound by the thresholds of the firehose (from below) and mirror (from above) instabilities, which rein the anisotropy at marginal stability (Schekochihin & Cowley 2006; Schekochihin et al. 2010; Kunz, Schekochihin, & Stone 2014; Sironi & Narayan 2015; Burgess et al. 2016; Riquelme, Quataert, & Verscharen 2016). In the case of small anisotropy, the limits are  $-2/\beta_{pl} < \Delta_e + \Delta_i < 1/\beta_{pl}$  (e.g., Kunz, Schekochihin, & Stone 2014). Due to a high  $\beta_{pl} \sim 100$  in the ICM, the net anisotropy (dominated by ions, as estimated above) presumably leads to ubiquitous generation of magnetic perturbations by ion (firehose and mirror) kinetic instabilities in regions with fluid motions. In addition to regulating the total anisotropy by scattering ions, these perturbations are able to enhance the electron collisionality as well, e.g., by magnetic mirroring (Komarov et al. 2016a). However, in regions where magnetic-field lines are stretched by large-scale fluid motions, as at the interface of a cold front,  $\beta_{pl}$  may be reduced sufficiently to avoid formation of the instabilities. We showed this in Appendix A of Paper I by comparing the calculated total anisotropies with the ion kinetic instabilities’ thresholds. This means, the reader should be aware of the fact that in those regions where the development of instabilities is predicted, the resulting SZ polarization signal could be reduced because of the higher effective electron collisionality. Electron instabilities, on the other hand, can also be triggered even if the electron anisotropy is rather small (see, e.g., Riquelme, Quataert, & Verscharen 2016, 2017, or in the case of a plasma with a temperature gradient (Levinson & Eichler (1992); Pistinner & Eichler (1998); Roberg-Clark et al. (2017); Komarov et al., in prep.). In all that follows, we assume that the electron anisotropy is unaffected by various instabilities and, thus, estimate the upper limit on the SZ polarization signal induced by the anisotropy.

The gyrotropic pressure anisotropy is commonly described by means of the bi-Maxwellian velocity distribution function:

$$f(v, \theta_0) = n_e \left( \frac{m_e}{2\pi T_{\perp}} \right) \left( \frac{m_e}{2\pi T_{\parallel}} \right)^{1/2} \times \exp \left[ -\frac{m_e v^2}{2T_0} \left( \frac{T_0}{T_{\perp}} \sin^2 \theta_0 + \frac{T_0}{T_{\parallel}} \cos^2 \theta_0 \right) \right], \quad (8)$$

where  $v$  is absolute value of the velocity,  $\theta_0$  is the angle

between the velocity vector and the symmetry axis (i.e., the magnetic field direction), and  $T_0 = (1/3)T_{\parallel} + (2/3)T_{\perp}$  is the mean temperature.

In the case of small anisotropy  $\Delta \equiv (T_{\perp} - T_{\parallel})/T_0$  we have  $\Delta m_e v^2 / (2T_0) \ll 1$  for the bulk of the electron population, so one can expand this distribution function to the first order in  $\Delta$  as

$$f(v, \theta_0) = f_0(v) + \delta f_{\Delta}(v, \theta_0), \quad (9)$$

where  $f_0(v)$  is an isotropic Maxwell distribution at temperature  $T_0$ :

$$f_0(v) = n_e \left( \frac{m_e}{2\pi T_0} \right)^{3/2} \exp\left(-\frac{m_e v^2}{2T_0}\right), \quad (10)$$

while the anisotropic part of the distribution is

$$\delta f_{\Delta}(v, \theta_0) = \Delta \frac{m_e v^2}{2T_0} \left( \frac{1}{3} - \cos^2 \theta_0 \right) f_0(v). \quad (11)$$

Defining  $\mu = \cos \theta_0$ , we rewrite this as

$$\delta f_{\Delta}(v, \mu) = -\Delta \frac{m_e v^2}{2T_0} f_0(v) P_2(\mu), \quad (12)$$

where  $P_2(\mu) = \mu^2 - 1/3$  is the Legendre polynomial of the second order, so this perturbation is of purely quadrupole nature, with the relative amplitude  $\delta f_{\Delta}(v, \mu)/f_0(v)$ , however, rising towards larger  $v$  as  $\propto v^2$ . As mentioned above, the actual anisotropy of the suprathermal electrons might turn out to be higher due to their lower collisionality compared to the bulk population ( $\nu_s \propto v^{-3}$ ), so the relative anisotropy amplitude might rise as  $\propto v^5$ . However, even if such scaling indeed takes place, it leads only to a factor of 1.3 increase in the predicted polarization signal (see Section 3).

### 3 SZ POLARIZATION

Let us consider the CMB radiation field with the intensity given by

$$I_{\nu}(x) = C \frac{x^3}{e^x - 1} \quad (13)$$

where  $x = h\nu/kT_{cmb}$ ,  $C = 2(kT_{cmb})^3/(hc)^2$ ,  $T_{cmb} = 2.725$  K,  $h$  is the Planck constant and  $c$  is the speed of light.

As was shown already by Sunyaev & Zeldovich 1980<sup>1</sup>, the presence of a quadrupole component in this incident radiation field  $I_{\nu}$  (as seen by an electron) gives rise to linear polarization of the scattered CMB radiation with the polarization degree

$$P_{\nu}(\mu') = \frac{1}{10}(1 - \mu'^2) \frac{I_2}{I_0}, \quad (14)$$

where  $I_0$  and  $I_2$  are the monopole and quadrupole amplitudes in the Legendre expansion of the incident radiation field  $I_{\nu}(\mu_0) = I_0 + I_1\mu_0 + I_2(\mu_0^2 - 1/3) + \dots$ , and  $\mu' = \cos \Theta = \mathbf{k}_z \cdot \mathbf{k}_f$  is the cosine of the angle between the quadrupole axis  $\mathbf{k}_z$  and the direction of the scattered photon  $\mathbf{k}_f$  (see Figure 1; Sunyaev & Zeldovich 1980). The

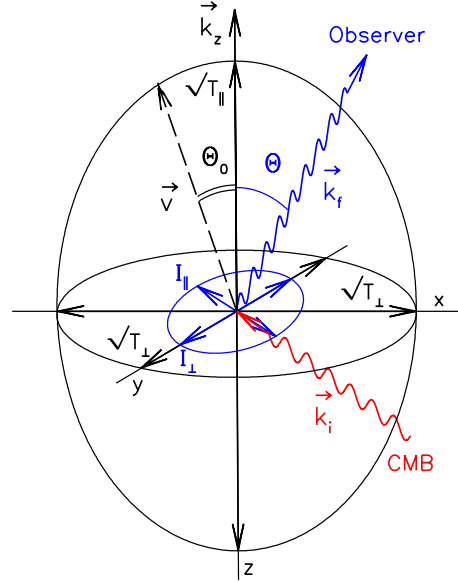


**Figure 1.** Illustration of the geometry of the problem. The incident CMB photon's direction is shown as  $\mathbf{k}_i$ , the direction of the scattered photon is  $\mathbf{k}_f$ ,  $\mathbf{k}_z$  is aligned with the system's symmetry axis, set either by the CMB quadrupole axis, or the velocity direction of an electron, or the magnetic-field direction in the case of a gyrotropic velocity distribution. In the latter case, the ellipsoid depicts an isoprobability surface in the velocity space, with the major and minor axis proportional to  $\sqrt{T_{\parallel}}$  and  $\sqrt{T_{\perp}}$ , respectively. The blue ellipse demonstrates the coordinate system in the picture plane of an observer, where  $I_{\parallel}$  and  $I_{\perp}$  correspond to photons with the electric-field vector oscillating along the projection of  $\mathbf{k}_z$  and perpendicular to it, respectively.

observed polarization vector will be aligned with the vector product of  $\mathbf{k}_z$  and  $\mathbf{k}_f$ , so it will be perpendicular to the projection of the quadrupole axis on the picture plane.

#### 3.1 Scattering of an intrinsic quadrupole

If there is an intrinsic quadrupole component in the angular power spectrum of the CMB corresponding to a temperature variance at level  $\delta T_q$ , the predicted polarization signal in the direction of a galaxy cluster with the Thomson optical depth  $\tau \sim n_e L \sigma_T$  will be

$$Q_{\nu,q}(x, \mu') = \frac{1}{10} \tau \frac{\delta T_q}{T_{cmb}} \varphi_0(x) I_{\nu}(x) (1 - \mu'^2), \quad (15)$$

where  $\sigma_T = 6.65 \times 10^{-25} \text{ cm}^2$  is the Thomson scattering cross section,  $n_e$  characteristic electron number density and  $L$  the size of the cluster (Sazonov & Sunyaev 1999). In this relation, the function

$$\varphi_0(x) = \frac{d \ln I_{\nu}(x)}{d \ln T} = \frac{x e^x}{e^x - 1} \quad (16)$$

describes the spectral dependence of the polarization fraction  $P_{\nu} = Q_{\nu,q}(x)/I_{\nu}(x)$ , while the factor  $1 - \mu'^2$  originates from the amplitude dependence on the position of the cluster on the sky.

The sky-averaged (rms) signal is

<sup>1</sup> In what follows, we will ignore relativistic corrections, which become important for gas temperatures above  $\gtrsim 10$  keV; see Challinor, Ford, & Lasenby (2000) and Itoh, Nozawa, & Kohyama (2000) for detailed discussions.

$$Q_{\nu, rms}(x) = \frac{\sqrt{6}}{10} \frac{Q_{rms}}{T_{cmb}} \tau \varphi_0(x) I_\nu(x), \quad (17)$$

where  $Q_{rms}$  is the rms amplitude of the quadrupole component. Since in the Local Universe it is measured (although with a large uncertainty) at the level of  $Q_{rms} \sim 10 \mu K$  (e.g., Bennett et al. 2003, 2013; Planck Collaboration et al. 2014), the corresponding CMB polarization is expected at the level of  $3\tau \mu K$  on average (while the maximum polarization is by a factor of  $\approx 1.7$  higher; Sazonov & Sunyaev 1999).

Thus, for a galaxy cluster with  $\tau \sim 10^{-2}$ ,  $Q_{rms}$  is expected at the level of  $\sim 25$  nK. Obviously, choosing not very distant galaxy clusters projected close to the direction of the CMB quadrupole axis should significantly decrease this effect, while its morphology could be easily predicted since it should closely follow the morphology of the cluster's optical depth.

### 3.2 Scattering on a moving electron

Let us now consider an electron moving with respect to the thermal radiation background with velocity  $v = \beta c$ , where  $c$  is the speed of light. Assuming that the background radiation field is isotropic and has a blackbody spectrum with temperature  $T_{cmb}$ , one can evaluate the spectral intensity of this radiation field as seen in the rest frame of the electron:

$$I_\nu(x, \mu_0) = C \frac{x^3}{e^{x\gamma_r(1+\beta\mu)} - 1}, \quad (18)$$

where  $\gamma_r = (1 - \beta^2)^{-1/2}$  and  $\mu_0$  is the cosine of the angle<sup>2</sup> between the electron's velocity vector and the direction of incidence of a photon (Sunyaev & Zeldovich 1980; Sazonov & Sunyaev 1999).

Expanding equation (18) in Legendre polynomials and keeping terms up to second order in  $\beta$  results in (Sazonov & Sunyaev 1999)

$$I_\nu(\mu_0) = C \frac{x^3}{e^{x\gamma} - 1} \left[ 1 + \frac{e^x(e^x + 1)}{6(e^x - 1)^2} x^2 \beta^2 - \frac{e^x}{e^x - 1} x \beta \mu_0 + \frac{e^x(e^x + 1)}{2(e^x - 1)^2} x^2 \beta^2 \left( \mu_0^2 - \frac{1}{3} \right) + \dots \right], \quad (19)$$

so the amplitude of the quadrupole term is

$$I_2(x) = I_0(x) \varphi_k(x) \beta^2, \quad (20)$$

with the quadrupole axis aligned with the electron's velocity direction, and the spectral dependence given by

$$\varphi_k(x) = \frac{e^x(e^x + 1)}{2(e^x - 1)^2} x^2. \quad (21)$$

Combining this with equation (14) gives

$$P_\nu(\mu') = \frac{1}{10} \varphi_k(x) \beta_t^2 (1 - \mu'^2), \quad (22)$$

where  $\beta_t = \beta \sqrt{1 - \mu'^2}$  is the projection of the electron's velocity on the plane of the sky. The electric field of the polarized emission is perpendicular to the projection of the electron's velocity on the plane of the sky.

<sup>2</sup> As measured in the rest frame of the electron. In any event, transformation from the electron's rest frame to the CMB (and observer's) rest frame results in changes of order higher than second in  $\beta$ , so we will neglect them here.

### 3.3 Anisotropy-induced polarization

The polarization of scattered emission considered above will vanish after the integration over isotropic electrons. If the distribution function is, however, not fully isotropic, some degree of polarization can be retained, and this is specifically the case for the gyrotropic distribution function considered in Section 2.

Indeed, let the symmetry axis of the system (set by the local magnetic-field direction) be aligned with the  $z$  axis, the  $y$  axis be perpendicular to both this direction and the direction toward the observer and the  $x$  axis lie in the same plane as the  $z$  axis and the line of sight (see Figure 1). Being perpendicular to the line of sight, the  $y$  axis lies in the picture plane, so we can use it as a reference axis for one of the Stokes parameters of the polarized emission, e.g.,  $Q$ . Clearly, the other axis is then aligned with the projection of the  $z$  axis on the picture plane. With such a choice of the coordinate system, the Stokes parameter  $U$  should cancel out as a result of the axial symmetry of the system (the Stokes parameter  $V$  is also zero because Compton scattering generates linear polarization only).

Let us define  $I_\perp$  as the intensity of the scattered radiation with the electric-field vector oscillating perpendicular to the projection of the  $z$  axis on the picture plane, i.e., along the  $y$  axis, and  $I_\parallel$  analogously, but with the electric-field vector oscillating parallel to it (see Figure 1). According to the considerations in Section 3.2, the contribution of an electron to  $I_\parallel$  is fully determined by the  $y$  component of its velocity  $v_y = \beta_y c$ :

$$P_{\nu, \parallel} = \frac{I_\parallel}{I_0} = \frac{1}{10} \varphi_k(x) \beta_y^2, \quad (23)$$

while the contribution to  $I_\perp$  is determined by the projections of its  $x$  and  $z$  velocity components,  $v_x = \beta_x c$  and  $v_z = \beta_z c$  on the picture plane, viz.,

$$P_{\nu, \perp} = \frac{I_\perp}{I_0} = \frac{1}{10} \varphi_k(x) (\beta_x^2 \cos^2 \Theta + \beta_z^2 \sin^2 \Theta), \quad (24)$$

where  $\Theta$  is the angle between the  $z$  axis and the direction towards the observer (see Figure 1).

Averaging these expressions over the axially symmetric electron distribution results in the substitution of  $\beta_x^2$ ,  $\beta_y^2$  and  $\beta_z^2$  by  $\langle \beta_\perp^2 \rangle$ ,  $\langle \beta_\perp^2 \rangle$  and  $\langle \beta_\parallel^2 \rangle$ , respectively, these averages being proportional to  $T_\perp$  and  $T_\parallel$ . The net polarization  $P_{\nu, a}(\mu') = P_{\nu, \parallel} - P_{\nu, \perp}$  is then given by

$$P_{\nu, a}(\mu') = \frac{1}{10} \varphi_k(x) (\langle \beta_\perp^2 \rangle - \langle \beta_\parallel^2 \rangle) \sin^2 \Theta, \quad (25)$$

where the positive sign of  $P_{\nu, a}(\mu')$  corresponds to the electric-field vector oscillating along the projection of the symmetry axis on the picture plane.

For a bi-Maxwellian electron distribution, one has  $\langle \beta_\parallel^2 \rangle / (T_\parallel / m_e c^2) = \langle \beta_\perp^2 \rangle / (T_\perp / m_e c^2) = \eta \approx 1.3$ , so the resulting polarization can be expressed as

$$P_{\nu, a}(\mu') = \frac{\eta}{10} \varphi_k(x) \Delta \frac{kT_0}{m_e c^2} (1 - \mu'^2), \quad (26)$$

where we have replaced  $\sin^2 \Theta$  by  $1 - \mu'^2$  for similarity with the expressions (15) and (22) for other effects. Allowing for the existence of a power-law dependence of the anisotropy in the high-energy tails of the electron distribution (see Section 2) increases  $\eta$  by a factor of 1.5 at most.

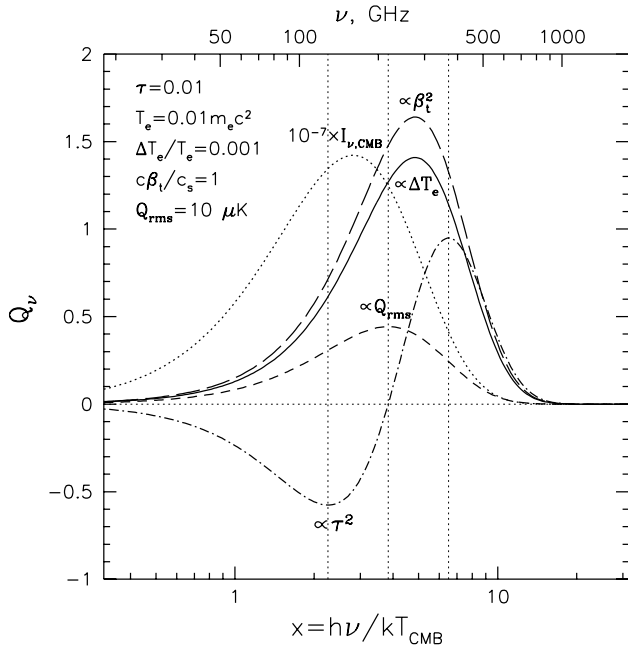


**Figure 2.** Relative amplitudes and spectral dependences of various polarization signals compared to the CMB intensity multiplied by  $10^{-7}$  (dotted line) for a cloud of electrons with temperature  $T_e = 0.01 m_e c^2 = 5.1$  keV, Thomson optical depth  $\tau = 0.01$ , electron pressure anisotropy  $\Delta T_e / T_e = 10^{-3}$ , and moving in the direction perpendicular to the line of sight with velocity  $\beta_t c$  equal to the adiabatic speed of sound in the cloud  $c_s = \sqrt{\gamma T_e / \mu m_p}$ ,  $\gamma = 5/3$  and  $\mu = 0.6$ , with respect to the CMB radiation field (characterized by quadrupole rms amplitude  $Q_{rms} = 10 \mu K$ ). The solid line shows polarization induced by pressure anisotropies, the long-dashed line by the kinematic SZ effect, the short-dashed line by scattering of the intrinsic CMB quadrupole, the dash-dotted line by second scatterings.

It is worth noting that only a large-scale observationally significant region of spatially correlated anisotropy in the ICM allows the combined polarization signal to be detectable. Any polarization produced by anisotropy fluctuations uncorrelated on scales much smaller than the size of a cluster (e.g., associated with turbulence) would be wiped out by integration along the line of sight. If the region of correlated anisotropies is characterized by the Thomson optical depth  $\tau_a$ , then the corresponding net polarization signal is

$$Q_{\nu,a}(\mu') = P_{\nu,a}(\mu') \tau_a I_\nu(x) = \frac{\eta}{10} \Delta \frac{k T_0}{m_e c^2} (1 - \mu'^2) \tau_a \varphi_k(x) I_\nu(x). \quad (27)$$

For mean electron temperature  $k T_0 = 0.01 m_e c^2 = 5.1$  keV and pressure anisotropy  $\Delta = 10^{-3}$ , the polarized signal is expected at the level  $\sim 35(\tau_a / 10^{-2})$  nK under geometrically most favourable conditions, i.e., when  $\mu' = 0$ . Thus, the anisotropy-induced polarization might turn out to be of the same order as the polarization induced by scattering of the primary quadrupole, as well as the polarization produced by the other effects considered in what follows.

### 3.4 Other sources of polarization

In addition to the two effects considered above (viz., scattering of the CMB quadrupole and the presence of pressure

anisotropies), there are a number of other effects capable of producing CMB polarization at approximately the same level. Namely, polarization arises due to the bulk motion of the cluster in the plane of the sky (kinematic SZ polarization) and due to scattering of the photons that have already scattered once off the electrons in the same cluster (called the  $\tau^2$  polarization because it is a second-order effect in  $\tau$ ). Besides that, polarization can be induced by the moving-gravitational-lens effect (Birkinshaw & Gull 1983; Birkinshaw 1989; Gibilisco 1997; Aghanim et al. 1998) and by the rotation of the cluster as a whole (Chluba & Mannheim 2002), but the corresponding signal is likely to be 1-2 orders of magnitude smaller (see Table 1), so we will not consider them here.

#### 3.4.1 kSZ polarization

Any bulk motions of the ICM (with respect to the CMB radiation field) that have a non-zero component in the plane of the sky also give rise to CMB polarization in that direction (Sunyaev & Zeldovich 1980). For an ICM region (e.g., a sub-cluster) with optical depth  $\tau_{kin}$  moving with bulk transverse velocity  $\beta_t$ , the polarization signal equals

$$Q_{\nu,k}(x) = \frac{1}{10} \beta_t^2 \tau_{kin} \varphi_k(x) I_\nu(x), \quad (28)$$

as follows directly from equation (22) (Sunyaev & Zeldovich 1980; Sazonov & Sunyaev 1999).

The characteristic scale of bulk motions is naturally set by the sound speed of the hot ICM  $c_s = \sqrt{\gamma k T_0 / \mu m_p}$ ,  $\gamma = 5/3$  and  $\mu = 0.6$ , so one has  $\beta_t = M c_s / c$  with the Mach factor  $M$  unlikely to exceed unity by a large factor (e.g., Dolag & Sunyaev 2013). Therefore, equation (28) can be rewritten as

$$Q_{\nu,k}(x) = \frac{1}{10} \frac{m_e}{m_p} \frac{\gamma}{\mu} M^2 \frac{k T_0}{m_e c^2} \tau_{kin} \varphi_k(x) I_\nu(x). \quad (29)$$

Comparing this with equation (26) gives

$$\frac{Q_{\nu,k}(x)}{Q_{\nu,a}(x)} = \frac{m_e}{m_p} \frac{\gamma M^2}{\eta \mu \Delta} \frac{\tau_a}{\tau_{kin}}, \quad (30)$$

where  $\tau_a$  and  $\tau_{kin}$  are the characteristic Thomson optical depths of the regions with correlated electron pressure anisotropies and bulk motions, respectively.

Clearly, for  $\Delta \sim 10^{-3}$  and  $M = 1$ , one has  $Q_{\nu,k}(x) \sim Q_{\nu,a}(x)$  if  $\tau_a \sim \tau_{kin}$ , so the two effects are expected to be of the same order of magnitude, i.e., at the level of  $\sim 15(\tau_k / 10^{-2})$  nK. This is particularly the case for galaxy clusters containing (super)sonic cold front substructures, as confirmed by the numerical simulations we present in Section 4 (see also Diego, Mazzotta, & Silk 2003 for simulations of kSZ-induced polarization for a similar setup).

Bearing in mind identical spectral dependences of the two effects and the fact that the bulk kinematic motions responsible for the polarization signal are not probed by the kSZ spectral distortions, since the latter are determined (in the leading order) by the line-of-sight velocities, one has to rely on morphological separation of the signals aided with the X-ray/SZ mapping of hydro- and thermodynamic properties of the particular system under consideration.

### 3.4.2 $\tau^2$ polarization

Another source of CMB polarization in the direction of galaxy clusters arises from the fact that the CMB sky appears distorted for the electrons inside a galaxy cluster due to scatterings by other electrons of the same galaxy cluster, i.e., due to scattering of the primary thermal or kinematic SZ distortions (Sunyaev & Zeldovich 1980; Sazonov & Sunyaev 1999; Lavaux et al. 2004; Shimon et al. 2006). As a result, this effect is second-order in the cluster's optical depth  $\tau$ . Spectral dependence of the polarization signal in this case corresponds to the spectral dependence of the primary SZ distortion, which for the thermal SZ is given by

$$\varphi_t(x) = \frac{xe^x}{e^x - 1} \left( x \frac{e^x + 1}{e^x - 1} - 4 \right), \quad (31)$$

while for the kinematic SZ effect it is given by equation (16) (Sunyaev & Zeldovich 1972, 1980).

For a homogeneous spherical cloud, the maximum intensity of the polarized emission is

$$Q_{\tau T, \nu}(x) = 0.014 \frac{kT_0}{m_e c^2} \tau^2 \varphi_t(x) I_\nu(x) \quad (32)$$

for the thermal effect, and

$$Q_{\tau K, \nu}(x) = 0.025 \sqrt{\frac{kT_0}{m_e c^2}} \sqrt{\frac{\gamma m_e}{m_p}} M \tau^2 \varphi_0(x) I_\nu(x) \quad (33)$$

for the kinematic effect (Sunyaev & Zeldovich 1980; Sazonov & Sunyaev 1999). The ratio of these two effects is

$$\frac{Q_{\tau K, \nu}(x)}{Q_{\tau T, \nu}(x)} = M \frac{\sqrt{\gamma m_e / m_p} \varphi_0}{\sqrt{kT_0 / m_e c^2} \varphi_t} \approx 0.3 M \sqrt{\frac{0.01}{kT_0 / m_e c^2} \frac{\varphi_0}{\varphi_t}}, \quad (34)$$

so the total  $\tau^2$  polarization is likely to be dominated by the scattering of the thermal SZ photons, except for frequencies close to  $x = 3.83$ , where the thermal effect changes sign. For a galaxy cluster with  $\tau \sim 10^{-2}$ , the corresponding polarization is expected at the level  $\sim 40(\tau/0.01)^2 nK$ , however, it has a distinct spectral shape as compared with the effects considered above.

For a non-spherically symmetric cluster, the contribution of this effect is likely to be enhanced, so that its morphology reflects the relative distribution of matter inside the cluster (Lavaux et al. 2004; Shimon et al. 2006). In Section 4, we will calculate the expected signal for a galaxy cluster with a cold front following the approach outlined by equations (25) and (26) in (Sazonov & Sunyaev 1999).

## 4 PREDICTIONS FOR A CLUSTER WITH A (SUPER)SONIC COLD FRONT

As we have shown in Section 3, there are a number of effects that lead to polarization of the CMB in the direction of galaxy clusters, although the predicted morphologies and spectral dependences of the signals are different. This situation is very well illustrated by the example of a galaxy cluster containing a (super)sonic cold front (Markevitch et al. 2000; Vikhlinin, Markevitch, & Murray 2001; Markevitch & Vikhlinin 2007). In this case, not only are significant bulk motions and asymmetries in the matter distribution present (which give rise to the kSZ and  $\tau^2$  polarization signals; see Diego, Mazzotta, & Silk 2003), but also magnetic-field stretching and sharp temperature gradients can occur,

which potentially seed electron pressure anisotropies (Paper I). In this section, we take advantage of the 3D MHD simulation of such a system presented in Paper I in order to predict qualitatively the amplitude and morphology of the anisotropy-induced CMB polarization in comparison with other polarization sources.

### 4.1 Numerical setup

Our numerical setup consists of a 3D box region of hot dilute plasma ( $T_{\text{out}} = 8 \text{ keV}$ ,  $n_{\text{out}} = 10^{-3} \text{ cm}^{-3}$ ) of spatial extent  $L = 1 \text{ Mpc}$  containing a colder spherical subcluster ( $T_{\text{in}} = 4 \text{ keV}$ ) of radius  $R = 200 \text{ kpc}$  at its center. The minimum linear scale captured by the simulation is  $\approx 2 \text{ kpc}$ . We use the same setup as in Paper I.

Initial density distribution inside this radius is given by a beta model,

$$n_{\text{in}} = n_c [1 + (r/r_c)^2]^{-3\beta'/2}, \quad (35)$$

with  $\beta' = 2/3$ , core radius  $r_c = R/\sqrt{3} \approx 115 \text{ kpc}$ , and central density  $n_c = 8n_{\text{out}}$ . The pressure balance is initially sustained by adding a gravitational acceleration field  $\mathbf{g}$  to mimic the effect of a static dark-matter halo at the center of the computational domain. The simulation is run in the reference frame where the subcluster is initially at rest, so it starts with the surrounding hot gas uniformly overflowing the subcluster with velocity  $v_0$ , which is set to the sound speed in the hot ambient plasma,  $c_{s0} = (\gamma p_{\text{out}}/\rho_{\text{out}})^{1/2} = (\gamma_{\text{gas}} kT_{\text{out}}/\mu m_p)^{1/2} \approx 1400 \text{ km/s}$ ,  $\gamma = 5/3$  and  $\mu = 0.6$ . Such a setup is similar to the one considered by Diego, Mazzotta, & Silk (2003), who focused on the kSZ polarization produced in this situation, and Asai, Fukuda, & Matsumoto (2007), whose main focus was on stretching of the magnetic-field lines at the cold front interface.

The evolution of the system is calculated by solving a standard set of MHD equations with anisotropic thermal conduction. As we aim at setting an upper limit on the CMB polarization, we use the unsuppressed Spitzer thermal conductivity in all our runs. In order to calculate the pressure anisotropy associated with thermal conduction, electron heat fluxes are obtained self-consistently by calculating temperature gradients along the magnetic field and multiplying them by the Spitzer thermal conductivity, which is a strong function of temperature. Note that at large temperature gradients, heat flux may become saturated when the characteristic parallel scale of the gradients becomes comparable with the Coulomb mean free path. However, by calculating the mean free path over the computational domain, we have found that it is sufficiently small practically everywhere (even at the cold-front interface due to magnetic-field draping), so that saturation should not play a noticeable role in the evolution of temperature. We therefore do not modify our expression for the heat flux to include saturation.

The initial magnetic field is set to be either uniform or random Gaussian with correlation length  $l_B = 100 \text{ kpc}$ , and its strength corresponds to the plasma beta  $\beta_{pl} = 200$  (in the case of a random field it is calculated with respect to the field dispersion  $B_0^2 = \langle B^2 \rangle$ ). We stress that the final magnetic field in the simulation with a random initial distribution does have non-Gaussian statistics due to the fact that it is a product of dynamical evolution in the velocity



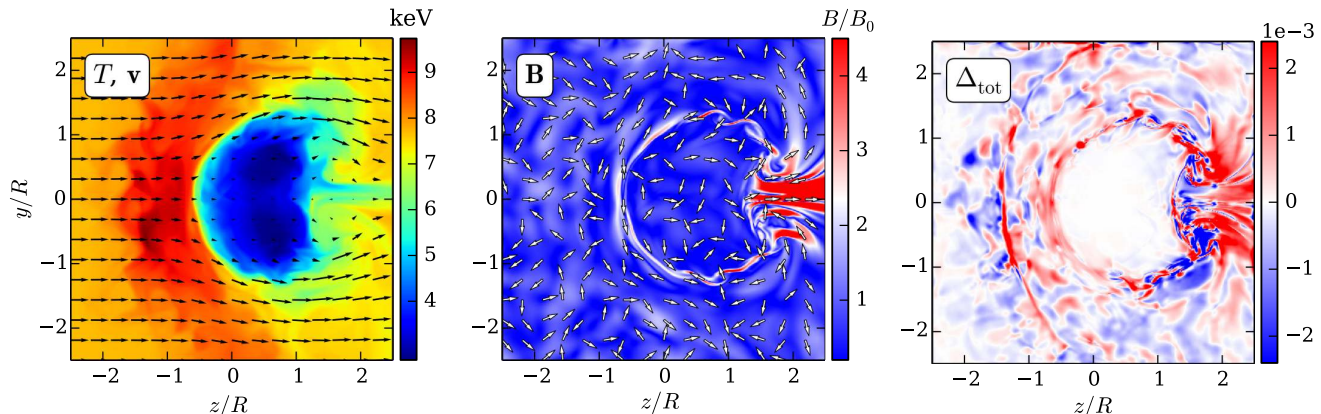


**Figure 3.** An illustration of the 3D MHD simulation with a random magnetic field (correlation length  $l_B \approx 100$  kpc) adapted from (Komarov et al. 2016b). All panels show a central slice of the computational domain (which is a 1 Mpc  $\times$  1 Mpc  $\times$  1 Mpc box) at the time  $t \approx 0.3$  Gyr after the start of the simulation. The left panel shows the temperature map (colour) and the velocity field (arrows). The magnetic field  $\mathbf{B}$  is shown in the middle panel (colour: field strength; arrows: unit vectors in the magnetic field’s direction projected onto the plane of the slice). The right panel shows the total generated pressure anisotropy defined relative to the local magnetic field’s direction, where plus sign corresponds to the perpendicular pressure exceeding the parallel pressure.

field of the cold front. The uniform-magnetic-field case is invoked mainly to highlight the regions where the largest pressure anisotropies can potentially arise in such a system. The run with a random magnetic field illustrates how this idealized picture would change in the more realistic situation of a turbulent ICM where magnetic fields are tangled by random fluid motions. The magnetic-field correlation length measured in the ICM is likely significantly shorter (see, e.g., Vogt & Enßlin 2005). However, we believe that already for  $l_B \lesssim R$ , when field loops can be folded up against the cold-front interface, our model is capable of capturing the qualitative changes in the predicted picture compared to the uniform field case. We expect to see a factor of  $\sim 2$  smaller polarization signal at the front in this case, because the random field lines are not oriented mainly perpendicular to the line of sight any more.

The resulting flow and magnetic-field structures are shown shown in Figure 3 for one central slice through the computational domain, where the three main features are clearly visible: a (weak) bow shock ahead of the subcluster, the cold-front interface, and the wake and backflow region that trails the main body of the subcluster. The generated pressure anisotropies are calculated according to equation (5), and the resulting distribution of anisotropies (for random magnetic field) is illustrated by the rightmost panel of Figure 3. The highest level of anisotropy is predicted in the wake region, where turbulent vortices amplify the magnetic field by stretching along the direction of subcluster’s motion (Asai, Fukuda, & Matsumoto 2007; Paper I).

## 4.2 Polarization calculation

The output of the simulations described above is then post-processed to obtain the predictions for corresponding CMB polarization signals, which are calculated locally for each effect in terms of the Stokes parameter  $dQ$  (according to expressions in Section 3), and then integrated along the line

of sight (over the extent of the computational domain) by the standard procedure (e.g., Lavaux et al. 2004):

$$\tilde{Q}_{\nu,a} = \int d\tau \frac{dQ_{\nu,a}}{d\tau} \cos(2\chi), \quad (36)$$

$$\tilde{U}_{\nu,a} = \int d\tau \frac{dQ_{\nu,a}}{d\tau} \sin(2\chi), \quad (37)$$

where  $\chi$  is the angle between the local polarization axis (see Section 3) and the reference polarization axis chosen globally on the observer’s picture plane (see, e.g., Figure 2 in Paper I).

For our calculation of the kSZ polarization, we assume that the hot gas overflowing the cold clump is actually part of a bigger cluster that is at rest with respect to the CMB radiation field. As a result, the unperturbed outer gas does not contribute to the kSZ polarization, and the latter is fully dominated by the subcluster’s contribution.

To calculate the  $\tau^2$  polarization, we first calculate it for a uniform box of a hot gas, with density and temperature equal to  $n_{out}$  and  $T_{out}$  respectively, and then subtract it from the  $\tau^2$  polarization calculated for the actual cold front setup. Both calculations are performed by evaluation of the CMB sky anisotropy due to the primary thermal SZ effect as seen by an electron at each particular point along the line of sight, and then integrating the resulting signal over the computational domain in the way similar to equations (36) and (37) (see Sazonov & Sunyaev 1999 for details).

It is worth mentioning that the predictions for the kSZ and  $\tau^2$  polarization differ only slightly between the uniform- and random-magnetic-field cases because the magnetic fields do not have a strong impact on the overall structure of the gas flow.

## 4.3 Predicted signal

As was shown in Section 3, various sources of polarization are characterized by different spectral dependences, so we produced maps of the predicted signal in three spec-



tral bands:  $x = 2.26$  (128 GHz),  $x = 3.83$  (218 GHz) and  $x = 6.51$  (370 GHz), at which the thermal SZ effect (and hence  $\tau^2$  contribution) has maximum decrement, changes sign and has maximum increment, respectively (see dotted vertical lines in Figure 2). The resulting spectrally resolved maps are shown in Figure 4 for partial contributions from various effects and in Figure 5 for the total predicted signal.

These results are consistent with the simple estimates presented in Section 3. The predictions for kSZ and  $\tau^2$  polarization are also in line with the results of previous numerical simulations (e.g., Diego, Mazzotta, & Silk 2003; Lavaux et al. 2004; Shimon et al. 2006). The partial contributions of these two effects are predicted at the level of  $\sim 10$  nK (see Figure 4), the total signal at the level of a few tens nK (see Figure 5). Notably, the amplitude of the anisotropy-induced polarization indeed turns out to be comparable with the amplitude of the kSZ and  $\tau^2$  polarization. However, these individual effects have either distinct morphologies of the signal in the observer's plane (e.g., kSZ polarization comes mainly from the gas of the subcluster, where anisotropy-induced polarization is negligible due to higher collisionality of the cold and dense plasma there), or distinct spectral shapes ( $\tau^2$  polarization vanishes at  $x = 3.83$ ), so one can hope to disentangle this complicated picture with the aid of high-angular-resolution and multi-frequency observations.

## 5 DISCUSSION

The results of the simulations presented in Section 4 confirm the basic predictions of Section 3: the electron pressure anisotropies potentially arising in the vicinity of a (super)sonically moving subcluster are capable of producing CMB polarization at the level comparable with the kSZ and  $\tau^2$ -induced signals.

### 5.1 Separating different sources of CMB polarization

This level corresponds to  $\sim 10$  nK in the Rayleigh-Jeans part of the spectrum, and it is also comparable to the expected level of polarization induced by scattering of the CMB's intrinsic quadrupole (see Section 3). The contribution of the latter effect might be additionally suppressed by selecting the only clusters that lie in the direction of the local CMB quadrupole axis. Also, using X-ray and tSZ observations of the same cluster, one can (with a certain accuracy) reconstruct the density (and temperature) distribution inside the cluster and then exploit it to predict the corresponding CMB polarization signal. The same is true for the  $\tau^2$  polarization, which can also be predicted based on the X-ray and tSZ maps of the cluster. Additionally, these two effects have spectral dependences different from kSZ and pressure-anisotropy-induced polarizations, so one can take advantage of multi-frequency observations to filter them out.

Separating the contribution of kSZ polarization appears to be the most challenging, since it has the same spectral dependence as the pressure-anisotropy-induced polarization. Also, it cannot be readily predicted from the observational data because it is determined by the difficult-to-measure transverse motions of the ICM plasma. In the case of a moderately supersonic motion of the subcluster, one may infer

its velocity from the density jump measured by the X-ray surface brightness mapping, although such an estimate is likely to be prone to projection and line-of-sight averaging effects (see, e.g., Markevitch et al. 2000; Vikhlinin, Markevitch, & Murray 2001). Besides that, by making this estimate one measures the subcluster's velocity relative to its ambient ICM, and not with respect to the CMB radiation field, and the latter (which is actually what needed) can differ from the former due to the (likely unknown) peculiar transverse motion of the cluster as a whole. Still, as we have shown in Section 4, the predicted morphologies of the kSZ and anisotropy-induced polarizations are significantly different, with the latter being almost absent in the direction of colder and denser plasma. Thus, high angular resolution observations will be helpful to separate these two effects, complemented by an adequately fine and sensitive X-ray surface brightness and temperature mapping. However, it is worth mentioning that high angular resolution is needed primarily for signal separation, rather than for detection of individual small-scale structures. Hence, the required sensitivity will be determined essentially by the signal integrated over regions of the correlated anisotropies.

Given that the collision rate goes down with the temperature, and, therefore, the anisotropy goes up, the anisotropy-induced polarization is expected to be significantly higher (at least as  $\propto \lambda_{mfp} T_e \propto T_e^3$  for fixed  $n_e$ ) in galaxy clusters that are more massive (and hotter) than the illustrative case considered here. Polarization signals due to other effects should also be higher in this case (because both optical depth and characteristic velocity of infalling subclusters should get higher as well), but their increase is likely to be less dramatic (e.g., as  $\propto \beta_t^2 \propto T_e$  for kSZ-induced polarization).

In addition to the CMB polarization caused by a galaxy cluster as described above, there are also primary fluctuations in CMB polarization at the angular scales of interest here ( $\sim 1$  arcmin, i.e.,  $l \sim 10^4$ ). These are significantly enhanced by gravitational lensing on the same cluster (or any intervening matter along the line of sight; see, e.g., Lewis & Challinor 2006). The expected amplitude of these fluctuations can be predicted based on our current knowledge of the CMB polarization power spectrum at larger scales and a mass model of the cluster, as has been extensively discussed in the literature (see, e.g., Amblard & White 2005; Liu, da Silva, & Aghanim 2005; Maturi et al. 2007; Shimon et al. 2009; Ramos, da Silva, & Liu 2012 for comparison of the level of these fluctuations with kSZ-induced polarization).

Secondary CMB polarization fluctuations generated during the re-ionization epoch should also contribute to the noise at these scales, but their level is likely to be orders of magnitude smaller (Hu 2000; Valageas, Balbi, & Silk 2001; Santos et al. 2003; Zahn et al. 2005). Potential contribution of point sources, e.g., lensed submillimetre galaxies (e.g., Lima, Jain, & Devlin 2010), is even harder to predict, but it can potentially be tackled by deep observations at wavelengths that are capable of revealing possible counterpart sources.

There are also a number of other possible sources of contamination, e.g., related to enhanced synchrotron emission due to the presence of a bow shock or scattering of radio emission of an AGN in one of the cluster's galaxies. This emission, however, typically has a spectral shape that

**Table 1.** Summary of various sources of CMB polarization in the direction of galaxy clusters. The polarization degree is expressed as  $P = P_0 \alpha(T, \tau, \beta_t, \dots) \varphi(x)$ , where  $P_0$  is the amplitude calculated for a fiducial set of parameters (see below),  $\alpha(T, \tau, \beta_t, \dots)$  the scaling of the amplitude with these parameters, and  $\varphi(x)$ ,  $x = h\nu/kT_{cmb}$ , describes the spectral dependence of the signal. The fiducial set of parameters is  $\tau = 0.01$ ,  $kT_e = 0.01 m_e c^2 = 5.1$  keV,  $\Delta T_e/T_e = 10^{-3}$ ,  $Q_{rms} = 10 \mu K$ ,  $\beta_t c = 1000$  km/s,  $\beta_r c = 100$  km/s,  $\Delta\theta = 1$  arcmin,  $D_l^{EE} = 0.1 \mu K$  at  $l = 10^4$ . Here,  $Q_{rms}$  is the rms amplitude of the local CMB quadrupole component (e.g., Bennett et al. 2003),  $\beta_t c$  the cluster’s transverse bulk velocity,  $\beta_r c$  the circular velocity due to rotation of the cluster (Chluba & Mannheim 2002),  $\Delta\theta = 4GM_{cl}/c^2 R \approx 0.7$  arcmin  $\left(\frac{M_{cl}}{10^{15} M_\odot}\right) \left(\frac{1 \text{ Mpc}}{R}\right)$  the angle of gravitational deflection of CMB photons by a cluster of mass  $M_{cl}$  at impact parameter  $R$  (Gibilisco 1997),  $D_l^{EE} = l(l+1)C_l^{EE}/2\pi$  the E-polarization power spectrum amplitude at  $l \sim 10^4$  (Lewis & Challinor 2006).

Effect causing polarization	Fiducial degree of polarization	Scaling	Spectral dependence	Reference
Pressure anisotropy	$\sim 10^{-8}$	$\propto \frac{\Delta T_e}{T_e} \frac{kT_e}{m_e c^2} \tau$	$\frac{e^x(e^x+1)}{2(e^x-1)^2} x^2$	Section 3.3
CMB quadrupole	$\sim 10^{-8}$	$\propto \frac{Q_{rms}}{T_{cmb}} \tau$	$\frac{x e^x}{e^x - 1}$	Section 3.1
Bulk motion (kSZ)	$\sim 10^{-8}$	$\propto \beta_t^2 \tau$	$\frac{e^x(e^x+1)}{2(e^x-1)^2} x^2$	Section 3.4.1
Second scatterings ( $\tau^2$ )	$\sim 10^{-8}$	$\propto \frac{kT_e}{m_e c^2} \tau^2$	$\frac{x e^x}{e^x - 1} \left(x \frac{e^x + 1}{e^x - 1} - 4\right)$	Section 3.4.2
Moving lens	$\sim 10^{-9}$	$\propto \beta_t \Delta\theta \tau$	$\frac{x e^x}{e^x - 1}$	Gibilisco 1997
Cluster rotation	$\sim 10^{-10}$	$\propto \beta_r^2 \tau$	$\frac{e^x(e^x+1)}{2(e^x-1)^2} x^2$	Chluba & Mannheim 2002
CMB fluctuations	$\sim 10^{-8}$	$\propto \frac{\sqrt{D_l^{EE}}}{T_{cmb}}$	$\frac{x e^x}{e^x - 1}$	Lewis & Challinor 2006

is very distinct from the CMB and is more easily observed at significantly lower frequencies ( $\lesssim 10$  GHz). Furthermore, there is likely to be contamination due to foreground polarized emission from the Galactic dust (e.g., Tucci et al. 2005), but this topic is far beyond the scope of our consideration here.

Certainly, the most promising technique would be to combine CMB polarization measurements with the measurements of polarization of X-ray emission both in lines (mainly from H- and He-like ions of heavy elements) and continuum (i.e., thermal bremsstrahlung emission), which should be sensitive to the same electron pressure anisotropies that determine the CMB polarization signal discussed here (Paper I). Besides that, pressure anisotropies in the distribution of the line-emitting ions might increase the broadening of these lines with respect to the broadening due to thermal and turbulent motions and resonant scattering. However, the collisionality of ions with charge  $Z$  is boosted by a factor  $\sim Z^{1.5}$  compared to protons, so the expected amplitude of pressure anisotropies is comparable (e.g., for silicon and sulphur,  $Z = 14 - 16$ ) or smaller (for iron,  $Z = 25 - 26$ ) then the amplitude of electron pressure anisotropies, i.e.,  $\sim 10^{-3}$ . Although both of these techniques are out of reach of current and forthcoming X-ray facilities, further improvements in polarimetric and calorimetric technologies will finally make such studies feasible, improving the possibility to study pressure anisotropy-induced CM polarization as well.

## 5.2 Effective electron collisionality

Detecting or constraining the CMB polarization associated with electron pressure anisotropies may allow one to extract valuable information about the microphysics of a high- $\beta$  plasma. If one knows the structure of the plasma flow (say, from current X-ray observations of cold fronts, or from the

future precise X-ray measurements of gas velocities via ion lines), and thus the rate of change of magnetic fields, it is possible to set lower limits on the electron collisionality. It is often believed that electron transport in the ICM is suppressed based on observations of significant temperature gradients in X-rays (e.g. Markevitch et al. 2000; Ettori & Fabian 2000; Vikhlinin, Markevitch, & Murray 2001; Vikhlinin & Markevitch 2002; Markevitch & Vikhlinin 2007). The exact mechanism of such suppression is yet to be understood, as it requires understanding of the intricate physics of a turbulent weakly collisional plasma.

The mirror instability caused by turbulent stretching of magnetic-field lines has been identified as one of the possible suppression mechanisms. However, the typical suppression factors in the ICM unlikely exceed a factor of 1/5 (Komarov et al. 2016a). In Appendix A of Paper I, we marked the regions where the mirror instability can be triggered by the plasma flow past a cold front due to generation of positive pressure anisotropies.

Another interesting suppression mechanism is a whistler instability triggered by a heat flux. It can be shown that in a weakly collisional high- $\beta$  plasma, even a small heat flux goes unstable and inhibits itself by triggering slowly propagating transverse magnetic perturbations (Levinson & Eichler (1992); Pistinner & Eichler (1998); Roberg-Clark et al. (2017); Komarov et al., in prep.). Nevertheless, large suppression factors are achieved only when the parallel temperature gradient scale approaches the electron mean free path, meaning for Knudsen numbers  $\gtrsim 0.1$ . Even in the case of cold fronts, where temperature gradients are the largest found in the ICM, parallel gradients turn out to be much smaller due to draping of the magnetic-field lines along the cold-front interface. We therefore conclude that currently, our understanding of the microphysics of a high- $\beta$  plasma does not allow one to predict very large suppression of electron transport confidently.

Conversely, if, somehow, one knows that electron transport is mediated by Coulomb collisions in a certain region of a cluster, it is possible to estimate the parallel velocity shear associated with the magnetic-field stretching rate.

## 6 CONCLUSIONS

We have predicted the CMB polarization in the direction of a galaxy cluster containing a (super)sonic cold front due to electron pressure anisotropies potentially generated by magnetic-field-line stretching and heat fluxes in the weakly collisional plasma of the ICM. The amplitude of this signal is predicted at the level of  $\sim 10$  nK in the Rayleigh-Jeans part of the spectrum, and it turns out to be comparable to the amplitude of kSZ and  $\tau^2$  polarization, as well as of the polarization due to intrinsic CMB quadrupole scattering for such a cluster.

With the aid of 3D MHD simulations of a cold front, we have demonstrated that the individual polarization effects have either distinct morphologies (e.g., the kSZ polarization comes mainly from the gas of the denser and colder subcluster, inside of which the anisotropy-induced polarization is negligible due to relatively higher effective collisionality of the gas), or distinct spectral shapes (e.g., the  $\tau^2$  polarization vanishes at  $x = 3.83$ ). As a result, one can hope to disentangle the resulting complicated picture by taking advantage of high-angular resolution and multi-frequency observations complemented by X-ray and spectral SZ data.

Measuring CMB polarization below  $1 \mu K$  currently presents an observational challenge. However, there is ongoing progress in available observational facilities, and also in our knowledge about various sources of contamination, and so accurately characterizing them is becoming more feasible. With further improvements, a detection of (or even an upper limit on) the pressure-anisotropy-induced polarization might become possible. This would provide a unique probe of the effective collisionality (as well as the effective thermal conductivity) of the ICM (paralleled perhaps only by X-ray polarization measurements, Paper I). More fundamentally, this will allow us to test the current understanding of the intricate physical processes animating ‘microscopic’ scales in the hot turbulent weakly collisional plasma of the ICM.

## ACKNOWLEDGEMENTS

We are grateful to the referee, Mark Birkinshaw, for the valuable suggestions that helped to improve the paper noticeably. IK, SK and EC acknowledge partial support by grant No. 14-22-00271 from the Russian Scientific Foundation. AAS was supported in part by grants from UK EPSRC and STFC.

## REFERENCES

Adam R., et al., 2016, *A&A*, 586, A122  
 Aghanim N., Prunet S., Forni O., Bouchet F. R., 1998, *A&A*, 334, 409  
 Amblard A., White M., 2005, *NewA*, 10, 417  
 Asai N., Fukuda N., Matsumoto R., 2007, *ApJ*, 663, 816

Bale S. D., Kasper J. C., Howes G. G., Quataert E., Salem C., Sundkvist D., 2009, *PhRvL*, 103, 211101  
 Bennett C. L., et al., 2003, *ApJS*, 148, 1  
 Bennett C. L., et al., 2013, *ApJS*, 208, 20  
 Birkinshaw M., Gull S. F., 1983, *Natur*, 302, 315  
 Birkinshaw M., 1989, *LNP*, 330, 59  
 Birkinshaw M., 1999, *PhR*, 310, 97  
 Bleem L. E., et al., 2015, *ApJS*, 216, 27  
 Burgess D., Hellinger P., Gingell I., Trávníček P. M., 2016, *JPIPh*, 82, 905820401  
 Carilli C. L., Taylor G. B., 2002, *ARA&A*, 40, 319  
 Carlstrom J. E., Holder G. P., Reese E. D., 2002, *ARA&A*, 40, 643  
 Challinor A. D., Ford M. T., Lasenby A. N., 2000, *MNRAS*, 312, 159  
 Chen C. H. K., Matteini L., Schekochihin A. A., Stevens M. L., Salem C. S., Maruca B. A., Kunz M. W., Bale S. D., 2016, *ApJ*, 825, L26  
 Chew G. F., Goldberger M. L., Low F. E., 1956, *RSPSA*, 236, 112  
 Chluba J., Mannheim K., 2002, *A&A*, 396, 419  
 Churazov E., Inogamov N., 2004, *MNRAS*, 350, L52  
 Diego J. M., Mazzotta P., Silk J., 2003, *ApJ*, 597, L1  
 Dolag K., Sunyaev R., 2013, *MNRAS*, 432, 1600  
 Etori S., Fabian A. C., 2000, *MNRAS*, 317, L57  
 Feretti L., Giovannini G., Govoni F., Murgia M., 2012, *A&ARv*, 20, 54  
 Gibilisco M., 1997, *Ap&SS*, 249, 189  
 Hasselfield M., et al., 2013, *JCAP*, 7, 008  
 Hellinger P., Trávníček P., Kasper J. C., Lazarus A. J., 2006, *GeoRL*, 33, L09101  
 Hu W., 2000, *ApJ*, 529, 12  
 Itoh N., Nozawa S., Kohyama Y., 2000, *ApJ*, 533, 588  
 Kasper J. C., Lazarus A. J., Gary S. P., 2002, *GeoRL*, 29, 1839  
 Kitayama T., et al., 2016, *PASJ*, 68, 88  
 Komarov S. V., Churazov E. M., Schekochihin A. A., ZuHone J. A., 2014, *MNRAS*, 440, 1153  
 Komarov S. V., Churazov E. M., Kunz M. W., Schekochihin A. A., 2016, *MNRAS*, 460, 467  
 Komarov S. V., Khabibullin I. I., Churazov E. M., Schekochihin A. A., 2016, *MNRAS*, 461, 2162  
 Kunz M. W., Schekochihin A. A., Stone J. M., 2014, *PhRvL*, 112, 205003  
 Lavaux G., Diego J. M., Mathis H., Silk J., 2004, *MNRAS*, 347, 729  
 Levinson A., Eichler D., 1992, *ApJ*, 387, 212  
 Lewis A., Challinor A., 2006, *PhR*, 429, 1  
 Lima M., Jain B., Devlin M., 2010, *MNRAS*, 406, 2352  
 Liu G.-C., da Silva A., Aghanim N., 2005, *ApJ*, 621, 15  
 Markevitch M., et al., 2000, *ApJ*, 541, 542  
 Markevitch M., Vikhlinin A., 2007, *PhR*, 443, 1  
 Maturi M., Moscardini L., Mazzotta P., Dolag K., Tormen G., 2007, *A&A*, 475, 71  
 Pistinner S. L., Eichler D., 1998, *MNRAS*, 301, 49  
 Planck Collaboration, et al., 2014, *A&A*, 571, A20  
 Planck Collaboration, et al., 2014, *A&A*, 571, A29  
 Planck Collaboration, et al., 2014, *A&A*, 571, A15  
 Ramos E. P. R. G., da Silva A. J. C., Liu G.-C., 2012, *ApJ*, 757, 44  
 Rephaeli Y., 1995, *ARA&A*, 33, 541

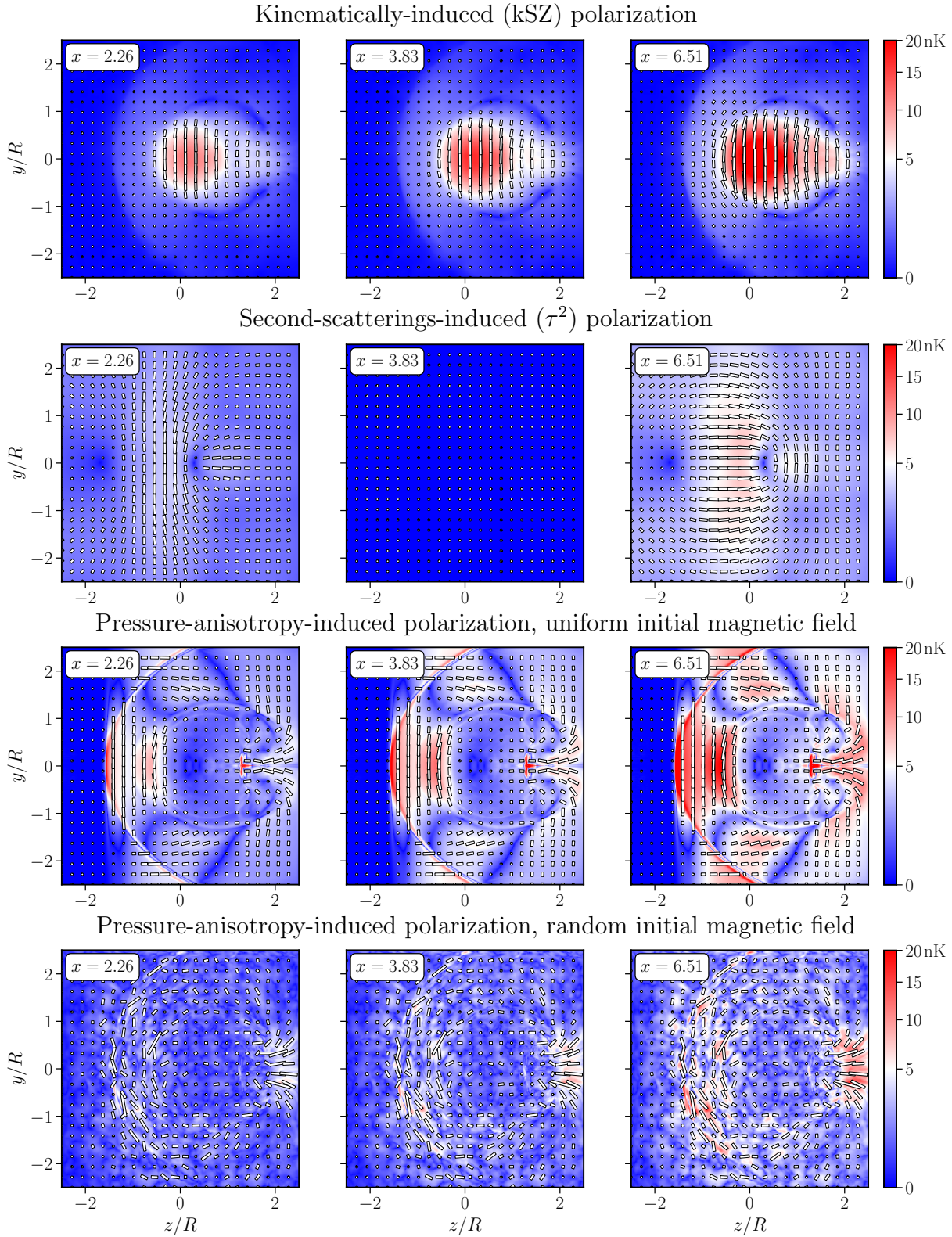


**Figure 4.** Various sources of CMB polarization in the direction of a galaxy cluster containing a (super)sonic cold front. The colour shows the amplitude of the signal (integrated along the line of sight over the computational domain), while the bars indicate the orientation of the polarization plane. Left panels correspond to frequencies around  $x = h\nu/kT_{cmb} = 2.26$ , middle panels to  $x = 3.83$ , right panels to  $x = 6.51$ . The top row shows the contribution of the kSZ-induced polarization, the row second from the top contribution of the  $\tau^2$  (i.e., induced by second scatterings) polarization, the row second from the bottom the contribution of the pressure-anisotropy-induced polarization in the case of a uniform initial magnetic field, the bottom row the contribution of the pressure anisotropy-induced polarization in the case of a random initial magnetic field.

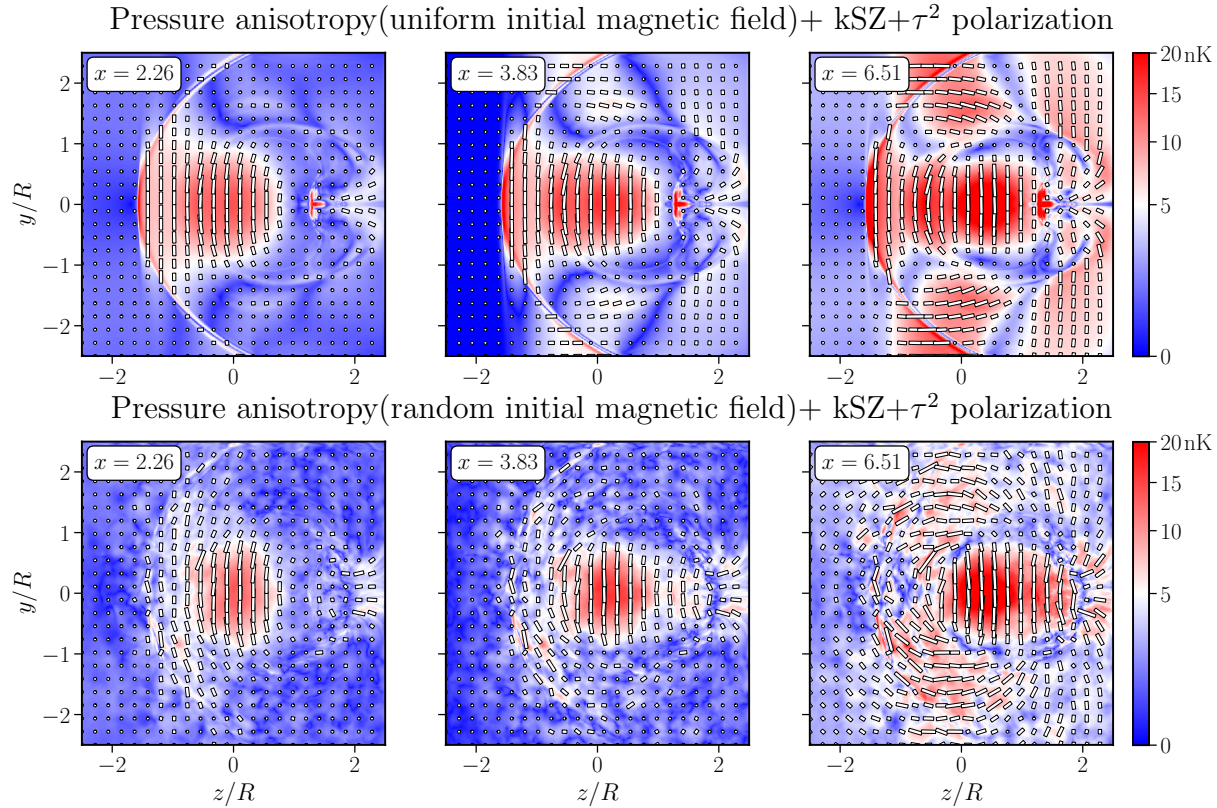


**Figure 5.** The same as Figure 4 but for the total predicted polarization signal for the uniform (upper row) and random (lower row) magnetic initial field configurations.

- Riquelme M. A., Quataert E., Verscharen D., 2016, *ApJ*, 824, 123
- Riquelme M., Quataert E., Verscharen D., 2017, arXiv, arXiv:1708.03926
- Roberg-Clark G. T., Drake J. F., Reynolds C. S., Swisdak M., 2017, arXiv, arXiv:1709.00057
- Rosin M. S., Schekochihin A. A., Rincon F., Cowley S. C., 2011, *MNRAS*, 413, 7
- Santos M. G., Cooray A., Haiman Z., Knox L., Ma C.-P., 2003, *ApJ*, 598, 756
- Santos-Lima R., Yan H., de Gouveia Dal Pino E. M., Lazarian A., 2016, *MNRAS*, 460, 2492
- Sarazin C. L., 1988, *X-ray Emission from Clusters of Galaxies*. Cambridge Univ. Press, Cambridge
- Sazonov S. Y., Sunyaev R. A., 1998, *ApJ*, 508, 1
- Sazonov S. Y., Sunyaev R. A., 1999, *MNRAS*, 310, 765
- Schekochihin A. A., Cowley S. C., Kulsrud R. M., Hammett G. W., Sharma P., 2005, *ApJ*, 629, 139
- Schekochihin A. A., Cowley S. C., 2006, *PhPl*, 13, 056501
- Schekochihin A. A., Cowley S. C., Rincon F., Rosin M. S., 2010, *MNRAS*, 405, 291
- Shimon M., Rephaeli Y., O’Shea B. W., Norman M. L., 2006, *MNRAS*, 368, 511
- Shimon M., Rephaeli Y., Sadeh S., Keating B., 2009, *MNRAS*, 399, 2088
- Sironi L., Narayan R., 2015, *ApJ*, 800, 88
- Spitzer L., 1962, *Physics of Fully Ionized Gases*, New York: Interscience (2nd edition)
- Štverák Š., Trávníček P., Maksimovic M., Marsch E., Fazakerley A. N., Scime E. E., 2008, *JGRA*, 113, A03103
- Sunyaev R. A., Zeldovich Y. B., 1972, *CoASP*, 4, 173
- Sunyaev R. A., Zeldovich I. B., 1980, *MNRAS*, 190, 413
- Sunyaev R. A., Zeldovich I. B., 1981, *ASPRv*, 1, 1
- Tucci M., Martínez-González E., Vielva P., Delabrouille J., 2005, *MNRAS*, 360, 935
- Valageas P., Balbi A., Silk J., 2001, *A&A*, 367, 1
- Vikhlinin A., Markevitch M., Murray S. S., 2001, *ApJ*, 549, L47
- Vikhlinin A. A., Markevitch M. L., 2002, *AstL*, 28, 495
- Vogt C., Enßlin T. A., 2005, *A&A*, 434, 67
- Young A. H., et al., 2015, *ApJ*, 809, 185
- Zahn O., Zaldarriaga M., Hernquist L., McQuinn M., 2005, *ApJ*, 630, 657
- Zeldovich Y. B., Sunyaev R. A., 1980, *SvAL*, 6, 285
- Zuhone J. A., Roediger E., 2016, *JPIPh*, 82, 535820301